Flow, Turbulence and Combustion
https://doi.org/10.1007/s10494-024-00558-y

RESEARCH

LES of Biomass Syngas Combustion in a Swirl Stabilised Burner: Model Validation and Predictions

Nikolaos Papafilippou[1] · Francesco Pignatelli[2] · Arman Ahamed Subash[3] · Muhammad Aqib Chishty[4] · Rikard Gebart[1]

Received: 27 November 2023 / Accepted: 6 June 2024
© The Author(s) 2024

Abstract
In this work, numerical investigations were performed using large eddy simulations and validated against detailed measurements in the CeCOST swirl stabilised burner. Both cold and reactive flow have been studied and the model has shown a good agreement with experiments. The verification of the model was done using the LES index of quality and a single grid estimator. The cold flow simulations predicted results closely to experiments setting baseline for the reactive simulations. Coherent structures like the vortex rope above the swirler and a precessing vortex core in the combustion chamber were identified. The reactive conditions were modelled with the Flamelet generated manifold and artificially thickened flame models. Simulations were performed for an experimental syngas composition from black liquor gasification at three different CO_2 dilution levels. Three different Reynolds numbers were investigated with the model matching closely to experimentally detected 2D flow field and OH for the most CO_2 diluted mixture. It was found that the opening angles of the flames differ by a maximum of 13% between experiments and simulations. The most diluted fuel investigated experienced a liftoff distance of 23.5 mm at the Re 25 k. This was also the highest liftoff distance experienced in this cohort of fuels. The same fuel also proved to have the thickest flame annulus at 78.5 mm. Overall, in cases with no experimental data available the predictions made by the model follow the same trends which hints its applicability to higher Re cases.

Keywords Biomass syngas · LES · Hydrogen combustion · CFD · FGM · Thickened flame model

✉ Nikolaos Papafilippou
nikolaos.papafilippou@associated.ltu.se

[1] Division of Energy Engineering, Luleå University of Technology, 97187 Luleå, Sweden

[2] Division of Fluid Mechanics, Department of Energy Sciences, Lund University, Lund, Sweden

[3] Division of Combustion Physics, Department of Energy Sciences, Lund University, Lund, Sweden

[4] Research Institutes of Sweden (RISE), Industrigatan 1, 94138 Piteå, Sweden

Published online: 18 July 2024

1 Introduction

Hydrogen fuels have recently been spiking the interest of both the scientific community and industry. A way to better handle these blends is by the addition of species such as CO_2, to reduce the risk of flashback. The interest in hydrogen and hydrogen blended fuels for power generation is motivated by the global drive for reduced greenhouse gas emissions. Of particular interest is to use these fuels in a combined cycle setup since this maximises the power efficiency and simplifies carbon capture (Lieuwen et al. 2009). However, most of the current commercial gas turbines are optimised for conventional hydrocarbons, e.g. methane, and therefore need improvements to increase the fuel flexibility of the combustor. In fact, methane flames behave very differently as compared to hydrogen and hydrogen-blended fuels, due to their thermal and chemical characteristics e.g., flammability limits (Lieuwen et al. 2009; Li et al. 2016; Samiran et al. 2017) and Lewis number (Lieuwen et al. 2009). Thus, hydrogen flames are diluted with inert species like CO_2, that can effectively reduce the high flame speed and temperature (Lieuwen et al. 2009; Li et al. 2016; Samiran et al. 2017), achieving a better control on the flame stabilization.

A promising alternative in an integrated gasification combined cycle plant is syngas from biomass gasification (Higman and van der Burgt 2008). Depending on the feedstock, gasification principle and the level of gas cleaning, the syngas from the gasification process can have a relatively large percentage of H_2 and it can also contain a significant fraction of CO (Higman and van der Burgt 2008; Carlsson et al. 2010; Taamallah et al. 2015; Papafilippou et al. 2022). The tendency of the flame to flashback increases with the H_2 content in the fuel mixture (Lieuwen et al. 2009; Samiran et al. 2017) and hence combustion behaviour with dilution is an important area of study.

This study focuses on validating a large eddy simulation (LES) model (Pitsch 2006) for different levels of CO_2 diluted syngas. Compared to a Reynolds Average Navier Stokes (RANS) or Unsteady RANS (URANS), LES is more computationally demanding. The small timestep needed to accurately resolve the temporal behaviour of the flame and to ensure numerical stability together with the fine mesh needed to resolve the spatial scales are two main factors that make LES modelling significantly more computationally demanding than the other two methods (Thierry Poinsot and Denis Veynante 2005). On the other hand, LES modelling has the advantage that, depending on the filter size, a large fraction of the turbulent scales is resolved, and that the influence from the sub grid scale models therefore is much smaller than the influence from the Reynolds stress models in RANS models (Pope 2000). Consequently, the modelling uncertainties in a properly resolved LES become much smaller than in RANS modelling. An additional advantage, in the context of combustion modelling, is that the resolved flame structure provides useful insights on the behaviour of different fuels during the combustion phase. Hence, accurate approximations become possible through LES, resolving the intricate dynamics of the flame (Endres and Sattelmayer 2018; Mira et al. 2018; Nicolai et al. 2022; Pillai et al. 2022).

This paper consists of an initial section that describes the investigated cases and the LES setup. This is then followed by a Results and Discussion section that encompasses a systematic description of the results and assessment of the test cases. The cold flow is first analysed and used to validate the fluid dynamics model by comparison against experiments. In the next step the reactive cases are analysed and compared against experimental results. Subsequently, predictions at higher Reynolds numbers are sought and assessed. Finally, the conclusions that can be drawn from the study are presented.

2 The CeCOST Burner Setup and Operating Conditions

The test case of the current study was the CeCOST swirl burner shown in Fig. 1. The inlet pipe section is 54 mm and is followed by an axial swirler, consisting of four quarter cones. The combustion chamber is 140 mm wide and 400 mm in height. The liner is made from quartz glass to give optical access to the flame in the combustor (Subash et al. 2020; Liu et al. 2021). At the end of the combustion chamber there is a sudden contraction, to provide controlled conditions at the outlet from the combustion chamber and to avoid backflow from the exterior. The swirl number S, defined in Eq. (1), is approximately 0.6 (Subash et al. 2020; Papafilippou et al. 2023; Pignatelli et al. 2023).

$$S = \frac{\int \overline{u}_k \overline{u}_j r^2 dr}{R \int \overline{u}_k^2 r dr} \tag{1}$$

where u_k and u_j are the mean axial and tangential velocities and R is the radius. The burner is located in a large room. Above the outlet of the burner, there is an exhaust duct that sucks in the products of combustion.

The syngas composition investigated in this paper is typical for oxygen blown black liquor gasification (Jafri et al. 2019). Black liquor is an energy rich byproduct of chemical pulping and is available in large quantities in countries that have forest product industry. The major species in the syngas mixture are CO, H_2 and CO_2, while the only significant minor species are CH_4 and H_2S at about 1–2% (Carlsson et al. 2010). The H_2S minor species must be removed before combustion (Higman and van der Burgt 2008), on the other hand methane should ideally be kept to maximise the heating value, which can be done with various techniques,

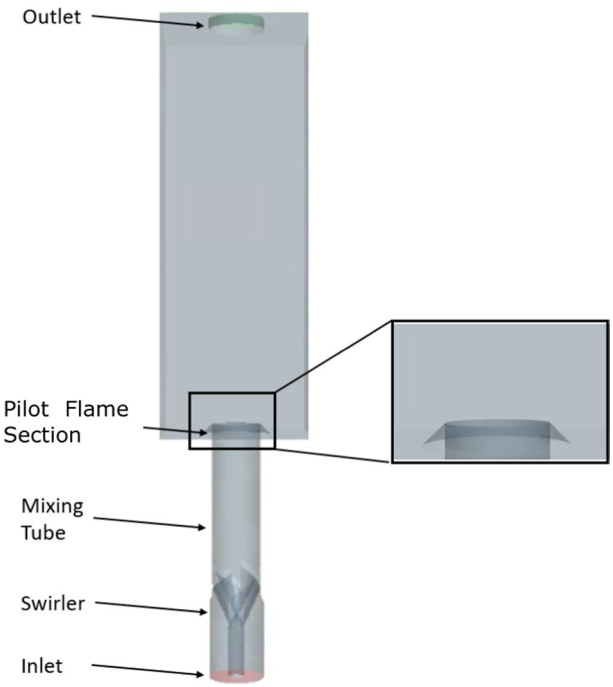

Fig. 1 CeCOST burner geometry

e.g. amine scrubbing (Landälv et al. 2014). The Wobbe index, describing the power input in a burner that changes with composition, of BLG syngas is only about one third of the Wobbe index for methane and natural gas, due to the high concentration of CO (Papafilippou et al. 2022). Hence, it is expected that the combustion behaviour of the black liquor syngas will be significantly different compared to the gaseous fuels that most of the existing gas turbines are designed for.

In practice, the untreated black liquor syngas contains roughly 34% carbon dioxide, but this can be adjusted by selectively removing a part or all the carbon dioxide in an amine wash or similar. In the rest of the paper the completely carbon dioxide free gas is termed undiluted while the other mixtures are termed diluted. Three different equivalence ratios were used for the three different concentrations of carbon dioxide. The equivalence ratios for these dilution cases were chosen to give nearly the same adiabatic flame temperature since this is an important parameter in gas turbine design. The syngas compositions for the three cases are shown in Table 1, where the SYN34 case corresponds to the untreated syngas from black liquor gasification (Carlsson et al. 2010). In order to clarify the effect of CO_2 dilution, Fig. 2 shows the laminar flame speed versus the equivalence ratio for all fuels. For a better assessment of the LES model, three Reynolds numbers (10 k, 20 k and 25 k) have been investigated, for all three dilutions. The available experimental results are in the range of Re 10 k for all cases and for Re 20 k for the SYN0 case. To ensure that the current model is following the experimental trends the Re 20 k cases of SYN15 and SYN34 were compared with SYN0. Subsequently, predictions were made for all cases at Re 25 k.

3 Numerical Modelling

LES modelling employs a filtered form of the governing Navier–Stokes equations, whereby a spatial filter is applied to separate grid and subgrid quantities. The Navier–Stokes equations hold true locally, in every computational control volume, as well as globally in the entire domain. Nominally, the equations are continuity (2), momentum (3), species transport (4) and the energy Eq. (5). In their filtered form (Thierry Poinsot and Denis Veynante 2005):

$$\frac{\partial \overline{\rho}}{\partial t} + \frac{\partial \overline{\rho}\tilde{u}_i}{\partial x_i} = 0 \tag{2}$$

$$\frac{\partial \overline{\rho}\tilde{u}_i}{\partial t} + \frac{\partial \overline{\rho}\tilde{u}_i\tilde{u}_j}{\partial x_i} = -\frac{\partial \overline{p}}{\partial x_j} + \frac{\partial}{\partial x_i}\left[\overline{\tau}_{ij} - \overline{\rho}\left(\widetilde{u_i u_j} - \tilde{u}_i\tilde{u}_j\right)\right] \tag{3}$$

$$\frac{\partial(\overline{\rho}\tilde{Y}_k)}{\partial t} + \frac{\partial(\overline{\rho}\tilde{u}_i\tilde{Y}_k)}{\partial x_i} = -\frac{\partial}{\partial x_i}\left[\overline{V_{k,i}Y_k} - \overline{\rho}\left(\widetilde{u_i Y_k} - \tilde{u}_i\tilde{Y}_k\right)\right] + \overline{\dot{\omega}}_k k = 1, 2, ..N \tag{4}$$

Table 1 Composition and properties of the different syngas fuel dilutions

Mixtures	CH_4 [%]	H_2 [%]	CO [%]	CO_2 [%]	Φ	T_{ad}/K
SYN0	3	53	44	0	0.47	1607.5
SYN15	2.55	45.05	37.4	15	0.5	1616.64
SYN34	2	35	29	34	0.56	1619.11

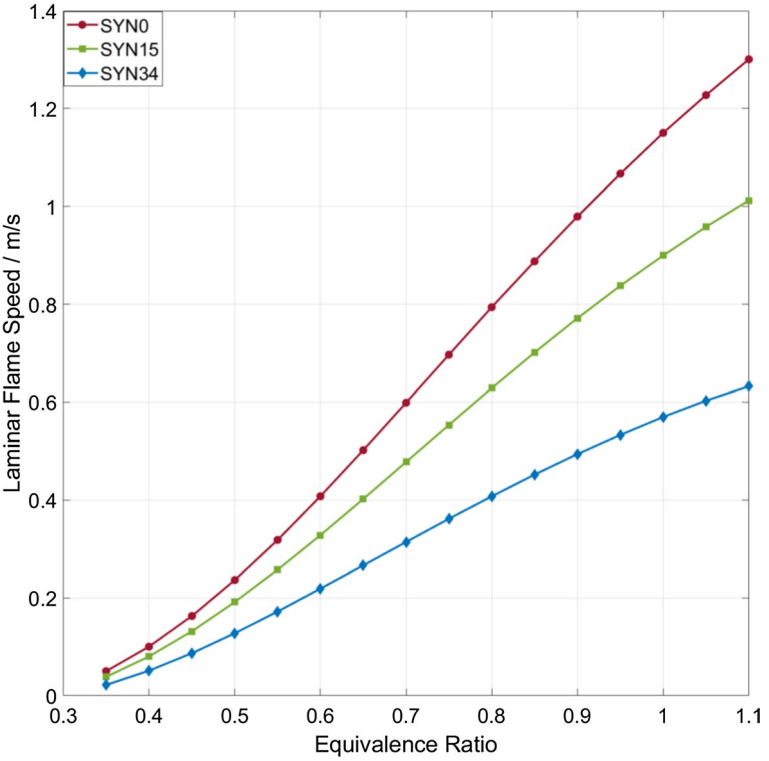

Fig. 2 Laminar flame speed versus equivalence ratio for all the fuels considered

$$\frac{\partial \overline{\rho}\tilde{h}_s}{\partial t} + \frac{\partial \overline{\rho}\tilde{u}_i\tilde{h}_s}{\partial x_i} = \overline{\frac{Dp}{Dt}} + \left[\overline{\lambda\frac{\partial T}{\partial x_i}} - \overline{\rho}\left(\widetilde{u_i h_s} - \tilde{u}_i\tilde{h}_s\right)\right] + \overline{\tau_{ij}\frac{\partial u_i}{\partial x_j}} - \frac{\partial}{\partial x_i}\left(\overline{\rho\sum_{k=1}^{N} V_{k,i}Y_k h_{s,k}}\right) + \overline{\dot{\omega}}_T \tag{5}$$

where ρ is the density, u is the velocity and Y_k is the mass fraction of species with index k ($k = 1, 2, 3, \ldots N$). The pressure is denoted by p and enthalpy by h, τ_{ij} is the viscous stress tensor. The filtered chemical reaction term of species k is denoted by $\dot{\omega}_k$ and a transport equation needs to be solved for each species. This process can be circumvented by pre-tabulating the chemical state. More about reactive flow modelling can be found in Sect. 3.1.

The commercial software STAR CCM+, version 15.06.008-R8 (Simcenter STAR-CCM+ User Guide 2020), based on a finite volume discretisation was used to solve the governing equations for all the simulations. A segregated flow model with a bounded central differencing scheme was chosen. The convection, enthalpy and time are subject to 2nd order discretisation (Ferziger et al. 2019). The geometry was discretised using a polyhedral grid, which uses a lower number of cells compared to a tetrahedral grid for the same accuracy (Ferziger et al. 2019; Simcenter STAR-CCM+ User Guide 2020), and which also simplifies the meshing of complex geometry features. It is worthy to note that all simulations herein are incompressible.

The closure model chosen was the dynamic Smagorinsky subgrid scale (SGS) model. The Dynamic Smagorinsky SGS model estimates subgrid scale dissipation from the

resolved scales, which is a significant improvement on the standard Smagorinski model (Thierry Poinsot and Denis Veynante 2005). The model constant C_s is estimated depending on time and space using the Germano identity. Second order approximations were used for the discretisation of all the equations. The walls had a no-slip condition via blended wall functions, which requires y + values in the range $1 < y+ < 30$. In addition, the temperature of the walls was set to room temperature. Since the liner of the burner is made from quartz glass this choice was assumed to be more appropriate than an adiabatic condition. The implicit unsteady model (Ferziger et al. 2019) was used with a timestep size of 5E-5 s and the total simulation time corresponded to ~5–6 flow-through times. The total simulated physical time of the cold flow case was 3.5 s. The mean Courant number in the vicinity of the swirler tip had a value of 3.9 (Re 10 k). This was the highest Courant number value in the simulation. In the mixing tube, the highest value of the mean Courant number was less than 2 and for the combustion chamber (area of interest) the highest value was 0.4. For the reactive simulations at Re = 10 k the mean Courant number values were similar to the cold flow results. For the higher Reynolds number cases (20 k, reactive) the highest mean Courant number was 10 at a few cells around the swirler tip with a drop in the mixing tube and a maximum value of 0.7 at the combustion chamber. The errors that arise by the CFL number in the vicinity of the swirler tip are expected to have negligible impact on the flame. It is assumed that the distance to the combustion chamber is enough in order to be smoothed out by turbulent processes. The outlet boundary condition was pure outflow for all the simulated cases. The inlet boundary condition was based on velocity (normal to the inlet plane), with 3 m/s for Re 10 k, and was appropriately adjusted for higher Re. In this work, no synthetic turbulence specification has been set. The total time needed for each simulation was 48–64 h on the Dardel supercomputer depending on Re, using approximately 300 cores. The total number of cells used in the simulations was approximately 6 million. Volume refinement controls were added around the swirler, mixing tube and the area of the flame to avoid high skewness, big Courant number jumps and to resolve the flame with reasonable accuracy. The cell size at the flame region was set to 1 mm. A view of the mesh and refinement levels on a mid-plane can be seen in Fig. 3.

3.1 Reactive Flow Modelling

For reactive modelling the flamelet generated manifold (FGM) model was used (van Oijen et al. 2016). This model pre-tabulates reaction data from kinetic, transport and thermodynamic files, speeding up simulations that require chemical schemes with a large number of reactions. FGM uses the mixture fraction, heat loss ratio and progress variable to parameterise the thermo-chemistry of the simulation (Thierry Poinsot and Denis Veynante 2005; van Oijen et al. 2016; Simcenter STAR-CCM + User Guide 2020). For the current setup the progress variable was defined based on the chemical enthalpy. For more information about FGM and a progress variable definition based on chemical enthalpy the readers are referred to reference (Lehtiniemi et al. 2006). To capture the flame propagation, the FGM model was coupled with the dynamically thickened flame (DTF) model (Legier et al. 2000; Thierry Poinsot and Denis Veynante 2005). DTF effectively thickens the flame front so the internal flame can be resolved on the mesh. Here, premixed laminar flame theory is used, where the laminar flame speed $S_l \propto \sqrt{\lambda \dot{\omega}}$ and the thickness $\delta_l \propto \frac{\lambda}{S_l}$ (Williams 1994). Increasing the thermal diffusivity, λ, and the laminar flame thickness, δ_l, by a factor of F while decreasing the reaction rate $\dot{\omega}$ by the same factor, artificially thickens the flame. In this way, the flame speed remains unaffected. To account for the effect of

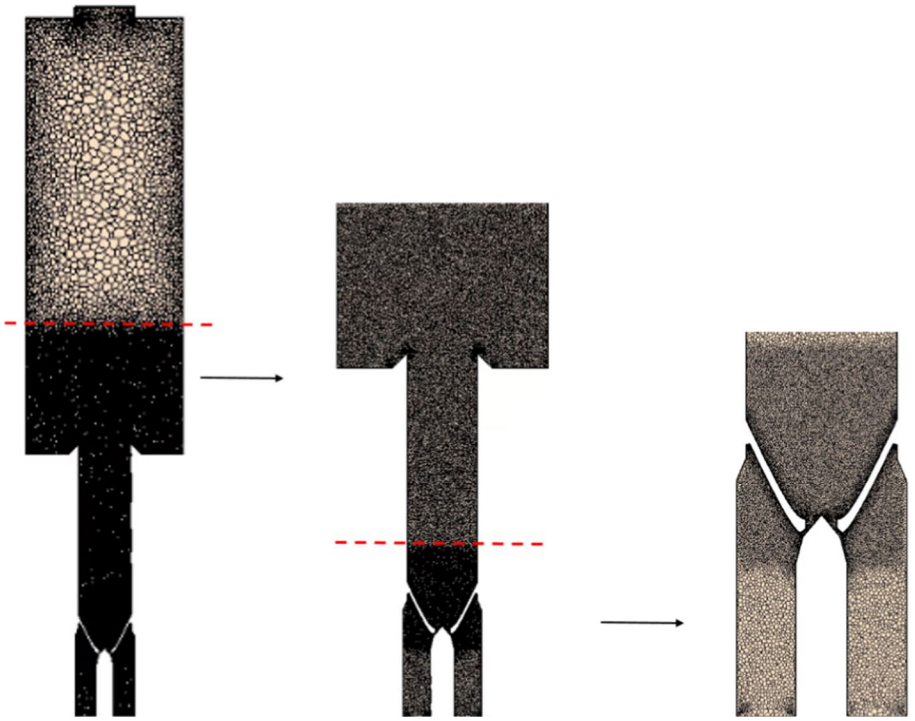

Fig. 3 Mesh refinement levels

turbulence wrinkling, an efficiency function, E, is used which was calculated based on a power law (Charlette et al. 2002). Both λ and $\dot{\omega}$ are increased based on E to account for subgrid scale wrinkling. Using this method, Eq. (5) is modified as:

$$\frac{\partial \overline{\rho}\tilde{h}_s}{\partial t} + \frac{\partial \overline{\rho}\tilde{u}_i\tilde{h}_s}{\partial x_i} = \overline{\frac{Dp}{Dt}} + \left[\overline{FE\lambda\frac{\partial \mathrm{T}}{\partial x_i}} - \overline{\rho}\left(\widetilde{u_i h_s} - \tilde{u}_i\tilde{h}_s\right)\right] + \overline{\tau_{ij}\frac{\partial u_i}{\partial x_j}} - \frac{\partial}{\partial x_i}\left(\overline{\rho\sum_{k=1}^{N} V_{k,i}Y_k h_{s,k}}\right) + \frac{\overline{F\dot{\omega}}_T}{E} \tag{6}$$

The artificial thickening could adversely affect the physics outside of the flame and to minimise this drawback, the thickening is only applied at the flame front by using a progress variable reaction zone sensor, Ω:

$$\Omega = tanh\left(16\beta[c(1-c)]^2\right) \tag{7}$$

where β is a model constant with a value of 100 and c is the normalised progress variable. Here, the progress variable source term is based on an Arrhenius expression (Thierry Poinsot and Denis Veynante 2005).

In the present setup, the thickening factor was chosen to let the internal flame structure to be resolved in 8 cells, with a maximum thickening factor of 20. The laminar flame speed $\left(S_L\right)$ that is needed in the turbulent flame speed model was approximated as a constant based on Cantera 1D (Goodwin et al. 2016) simulations and the laminar flame thickness was calculated assuming a power law thermal diffusivity:

$$\delta_L^o = 2\frac{D_u}{S_L^o}\left(\frac{T_b}{T_u}\right)^{0.7} \tag{8}$$

where D_u is the unburnt thermal diffusivity and where T_b and T_u are the burnt and unburnt temperature respectively. The inclusion of radiative heat transfer in the model is expected to lower the peak temperature a couple hundred degrees Kelvin (Papafilippou et al. 2022). However, it has been omitted in the present study due to its computational demand.

The initial condition for the cold flow case was a zero-velocity field. For the reactive cases, converged mean velocity data from the cold flow were used as initial conditions to speed up the simulation. The inlet boundary condition for all simulated cases was a uniform axial velocity inlet, upstream of the swirler guide vanes. The chemical reaction mechanism used in this study was the GRI-Mech 3.0 detailed chemical scheme that includes 53 species and 325 reactions (GRI-Mech 3.0, no date). This scheme was originally developed for methane but has been successfully used for syngas combustion (Lieuwen et al. 2009; Samiran et al. 2019; Papafilippou et al. 2022).

3.2 Convergence to Steady State

A number of monitoring points were placed in areas of high gradients (flame front for the reaction case) to estimate convergence. Convergence was assumed to be achieved when the running average of the mean axial velocity (U_{mean}) for the cold flow case and axial velocity and mean OH mole fraction (OH_{mean}) for the reactive flow case as well as their RMS values (U_{RMS} and OH_{RMS}), approached a stationary value. Data acquisition started after approximately 2.5 flow through times to account for initial noise. In addition, within each time step all simulation residuals were required to drop at least 3 orders of magnitude. Figures 4 and 5 show the normalised cumulative averages of the mean axial velocity and normalised RMS-values in one of the monitor points for cold, and reactive flow respectively. The x-axis is the time normalised by the flow-through time (the ratio of the total volume and the volumetric flow rate into the domain).

3.3 Solution Verification

The solution verification was done a posteriori, however, to avoid disrupting the flow of results in the next session it is discussed here. LES verification is a complex topic with no clear and universally applicable method for quality prediction (Gicquel et al. 2012). This stems from the interlinkage between the discretization and modelling errors (Freitag and Klein 2006). Many methods have been proposed, such as the systematic grid and model variation (SGMV) (Klein 2005; Freitag and Klein 2006), the five equation model (Dutta and Xing 2018), the subgrid activity parameter (Geurts and Fröhlich 2002; Meyers et al. 2003), the Mesh Quality Criterion (Vervisch et al. 2010) and the LES index of quality (LES_IQ) (Celik et al. 2005, 2009). The SGMV and the five equation model require many grids for the assessment, and for this work the additional computational time needed makes them impractical. The Subgrid Activity Parameter requires fewer grids but is difficult to evaluate, and it is based on the standard Smagorinsky model, meaning that ad-hoc modifications would be needed for the current work (Geurts and Fröhlich 2002; Celik et al. 2009). The LES_IQ is a more straightforward method and easier to use than the Mesh Quality Criterion for a commercial software and was therefore

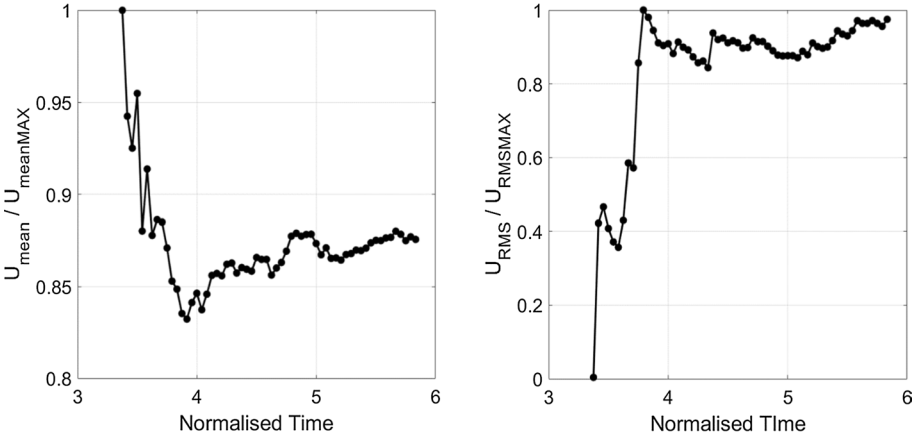

Fig. 4 Cold flow convergence. Left: mean axial velocity. Right: axial velocity RMS values

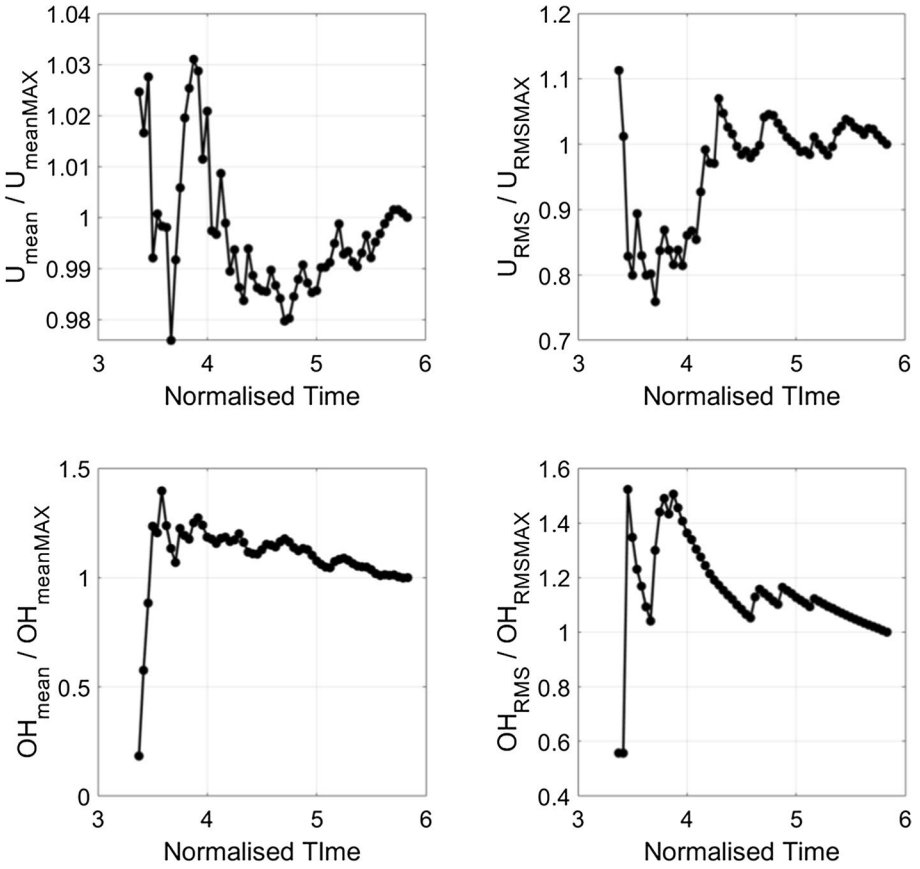

Fig. 5 Reactive flow convergence. Top: axial velocity convergence, bottom: OH mole fraction convergence

chosen as the verification measure. However, LES_IQ is also accompanied by its own drawbacks and difficulties. It involves empirical relations which have been reported to not be well tested (Dutta and Xing 2018). In addition, it performs poorly close to walls where the flow is laminar/transitional due to the TKE being close to zero, especially when a Germano based SGS model is under consideration (Klein 2005). For clarity, the LES_IQ does not provide a quantification or errors, but rather how far the LES lies from a DNS based on the criterion of resolved energy (Pope 2000). Note that the authors do not aspire to critique the different verification methods found in literature but rather to set the scene, decision, advantages, and drawbacks of a specific tool used.

$$LES_IQ = \frac{k^{res}}{k^{tot}} = \frac{k^{res}}{k^{res} + a_k h^p} \tag{9}$$

$$LES_IQ = 1 - \frac{|k^{tot} - k^{res}|}{k^{tot}} \tag{10}$$

In Eqs. (9) and (10), k^{res} is the resolved Turbulent Kinetic Energy (TKE), k^{tot} is the total TKE, a_k is a coefficient dependent on grid size and the resolved TKE from two grids, h is the global grid index parameter, p is the order of the scheme. The term $a_k h^p$, in the denominator of Eq. (9), represents the numerical and SGS model TKE contribution. Equation (9) is the general form of the LES_IQ, Eq. (10) is the form used in the case of oscillatory convergence as there are occasions where the coarse grid has been reported to resolve more of the TKE than the fine grid for unclear reasons (Celik et al. 2005). The case discussed here is no different, experiencing oscillatory convergence and sub-optimal index values close to walls and near the swirler. Figure 6 shows the LES_IQ distribution on a cross section plane of the numerical domain, which has been clipped to be in the range of 0.75–1. The TKE in the area upstream of the swirler is nearly zero, similarly very low values are encountered in the combustion chamber away from the refinement area / flame zone. The index values around the swirler and mixing tube, as well as the index values close to the walls of the refinement area do not make the cutoff of 75% suggested by Celik (Celik et al. 2005) and it is assumed this is due to the aforementioned difficulties in verifying LES simulations. Nonetheless, in the flame refinement zone (excluding parts of the ORZ) where good resolution is crucial, the LES_IQ lies in the required range for a good LES (75% > LES_IQ > 95%).

In addition, the apparent order of the scheme (Celik et al. 2009) was calculated to 1.67 from:

$$p = \frac{ln\left(\frac{k^2_{sgs}}{k^1_{sgs}}\right)}{ln\left(\frac{h_2}{h_1}\right)} \tag{11}$$

where the k_{sgs} is the subgrid scale TKE and the superscripts 1 and 2 refer to the coarse and fine grid, respectively. This value is a reasonable result since the formal order of the numerical scheme is 2. As an alternative quality assessment of the results and in hope of eliminating the influence from oscillatory convergence a single grid estimator based on (Celik et al. 2009) was also used:

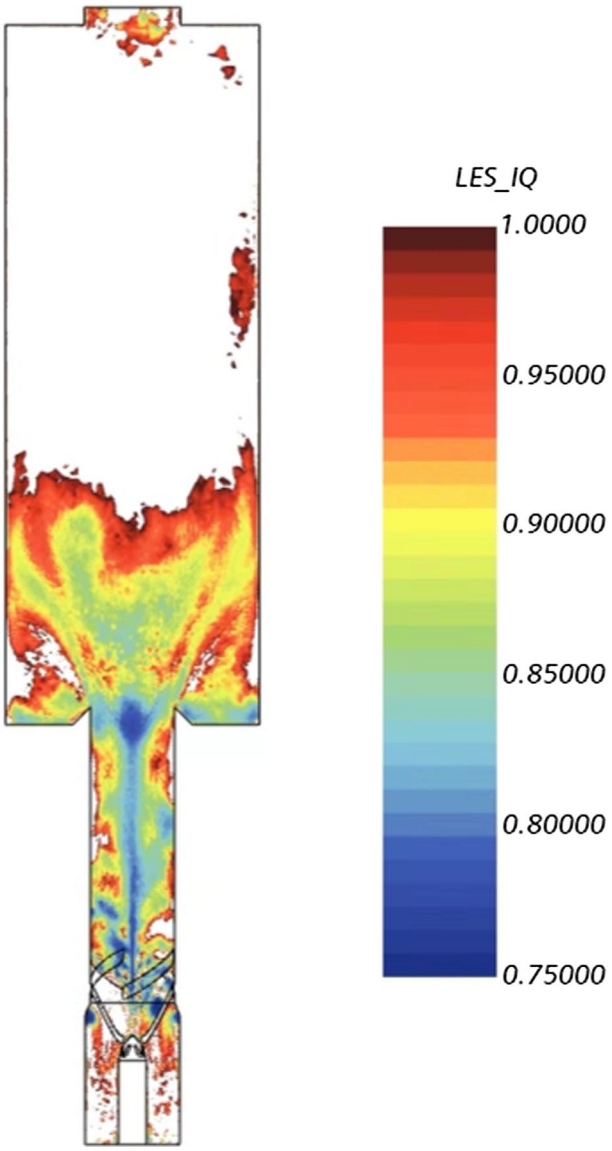

Fig. 6 LES_IQ for the SYN0 case at Re 10 k

$$\frac{k_{res}}{k_{tot}} = \frac{k_{res}}{k_{res} + k_{tot} + |k_{num}|} \tag{12}$$

where k_{num} is approximated as in (Celik et al. 2009), assuming equal weightings of numerical and modelling errors. This yielded significantly improved results both in index values and in the form of a proper scalar field (Fig. 7). Problematic areas still exist, such as the walls near the swirler, swirler blades and part of the outlet. The non-satisfactory resolution at the outlet is of no consequence for the flame dynamics since the upstream influence from errors at the outlet is extremely weak in a strongly convective flow. On the other hand,

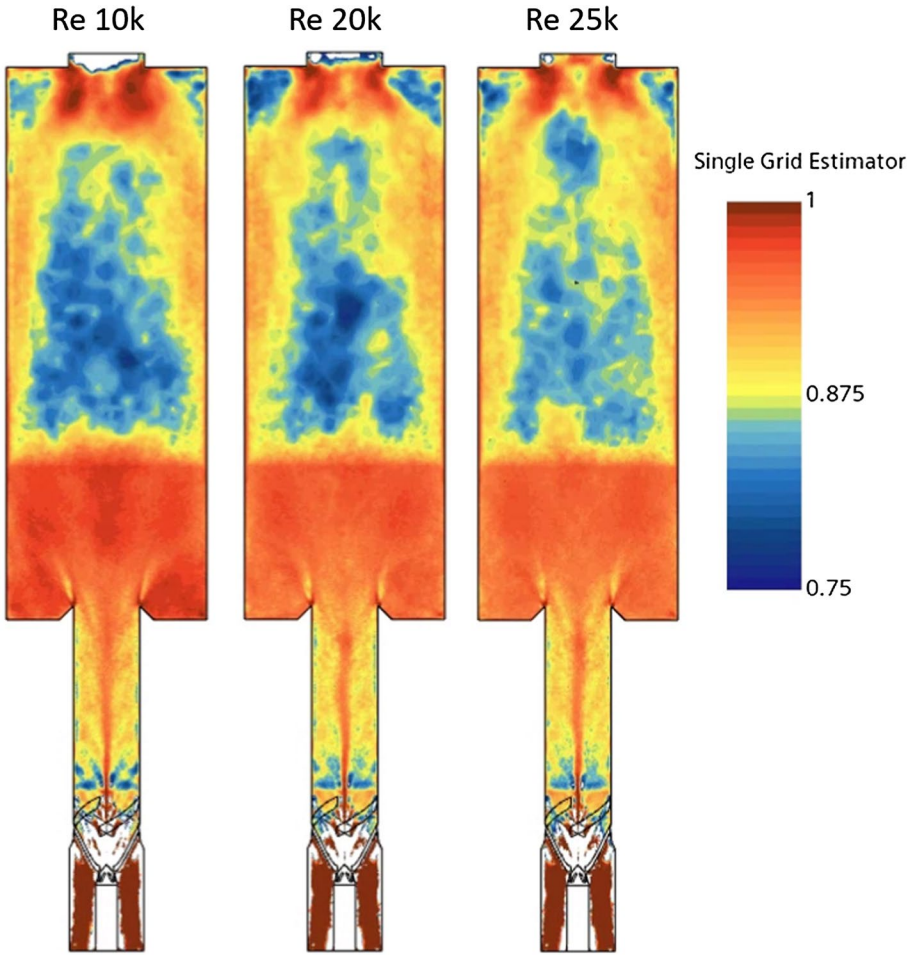

Fig. 7 Single grid estimator values for SYN0 for all Re

the model errors from the guide vanes will have some influence downstream. However, the dynamics of the turbulent flow will quickly erase this influence and instead establish a balance between the various turbulent processes, e.g., production and dissipation, that is independent of small perturbations upstream. Nevertheless, to provide a reasonable index, the single grid estimator was used for all Reynolds numbers, reactive flow for SYN0. The rest of the cases are assumed to behave similarly to SYN0 at their respective Reynolds numbers.

4 Results and Discussion

The model assessment was done in two steps. In the first step the fluid dynamics model, without reaction modelling was compared against cold flow experiments to make sure that the agreement was reasonable. This is a necessary requirement since it would be

meaningless to compare the combustion model against experiments if the fluid dynamics were poorly predicted. In the second step the complete model was validated against an experimental parametric study (Pignatelli et al. 2023) to appraise the accuracy that can be expected from the model. After the assessment against experiments, the model was used to explore the behaviour of the burner for operating conditions with no experimental data available.

4.1 Cold Flow Results

The experiments were performed on the latest version of the CECOST burner (Pignatelli et al. 2023) using air at room temperature as oxidiser with a Reynolds number of 10,000, based on the diameter of the premixing pipe, the viscosity of air, and the bulk axial flow speed of the mixture at the exit of the premixing pipe.

A comparison with experimental velocity data is shown in Fig. 8. The velocity values were normalised with the inlet velocity below the swirler guide vanes. As can be seen in Fig. 8, where the axial velocity profile is plotted for four different heights above the dump plane, the simulation and experimental results are in good agreement.

The general trends and the positions of the positive and negative axial velocity peaks are excellently predicted. However, the magnitude of the peak velocity is over-predicted, which due to continuity led to an under prediction of the velocity at the outer edges. It should also be remembered that experimental uncertainties may have a noticeable effect when comparing experimental results with numerical predictions. The experimental errors

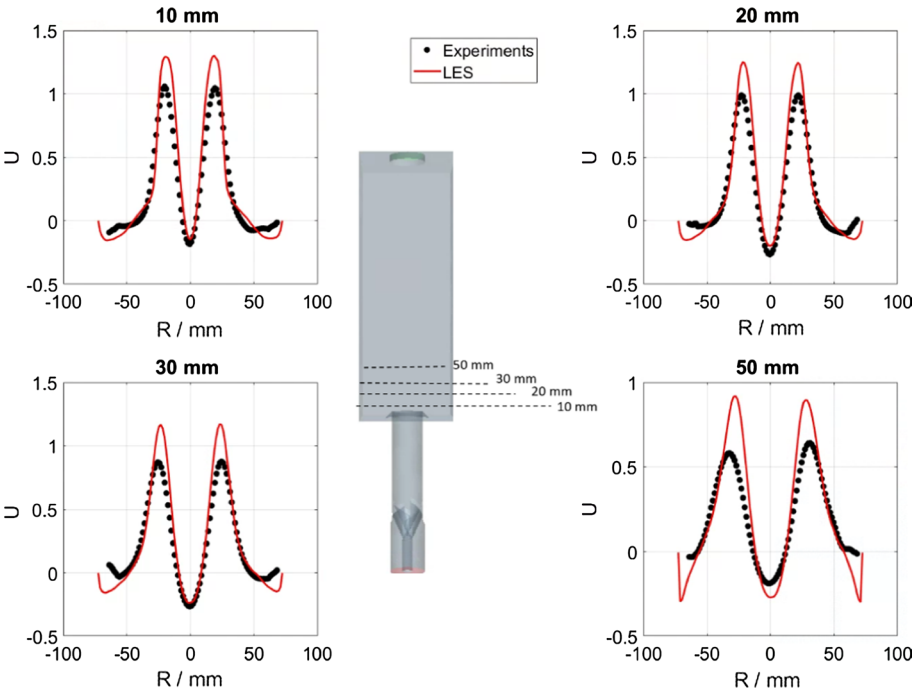

Fig. 8 Averaged axial velocity comparison of LES and experiments at different axial positions

in the PIV measurement were minimised by careful adjustment of the experimental setup and by following the data evaluation procedure that is described in (Pignatelli et al. 2023).

In Fig. 9 the dimensionless horizontal velocity is compared (normalised by inlet velocity). Similar to the averaged axial velocity, the peaks and troughs at different positions are predicted excellently by the simulations. Notice, that the experimental values are not perfectly antisymmetric as would be the case if the flow field was rotationally symmetric. The reason is most likely due to experimental uncertainty. However, the simulation results are much closer to perfect antisymmetry as a result of the perfect symmetric geometry and boundary conditions in the simulation. Overall, the cold flow comparison indicates that the turbulence model is sufficiently accurate to be used as the basis for the combustion model.

Figure 10 shows the corresponding contour plots of the averaged velocity components i.e., axial, radial, and tangential. Averaging started after 1.5 s to allow the solution some time to dampen the influence from the constant value starting guess. Subsequently, the initial transient cumulative averages were computed during more than 3 flow through times. Increasing the sampling time could potentially improve the agreement with experimental data at higher axial positions. Nonetheless, due to the overall good agreement this was deemed unnecessary.

Notice that the flow in the domain is purely axial with zero radial and tangential velocity before the swirler guide vanes. When the flow meets the guide vanes, a turbulent swirling flow is generated, which propagates into the combustion chamber where it develops into a complicated flow pattern. Most noticeable are the inner recirculation zone (IRZ) and the outer recirculation zone (ORZ), which are hinted at by the isolines for zero axial velocity in

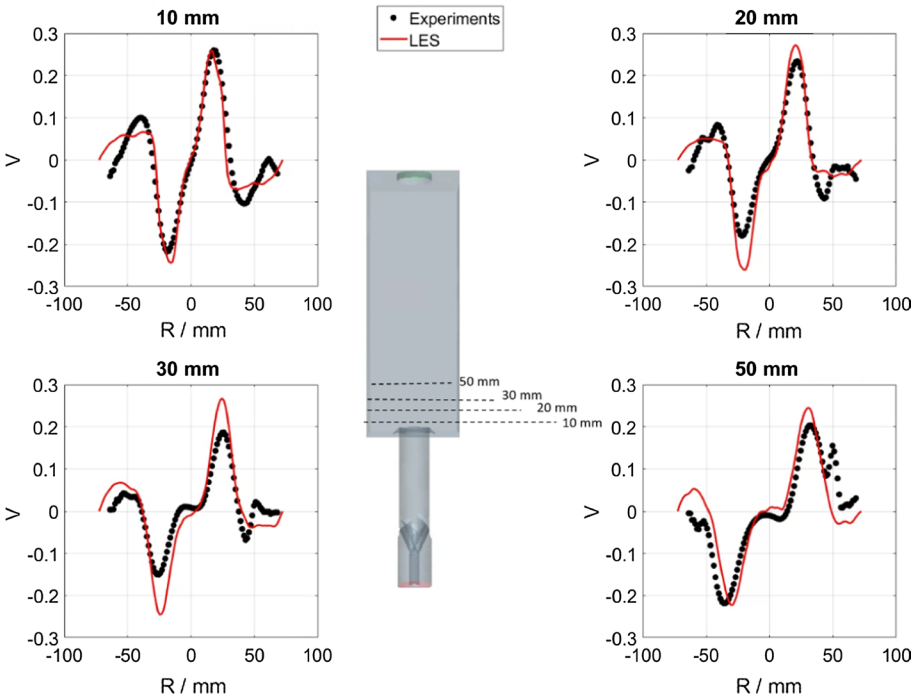

Fig. 9 Averaged horizontal velocity comparison of LES and experiments at different axial positions

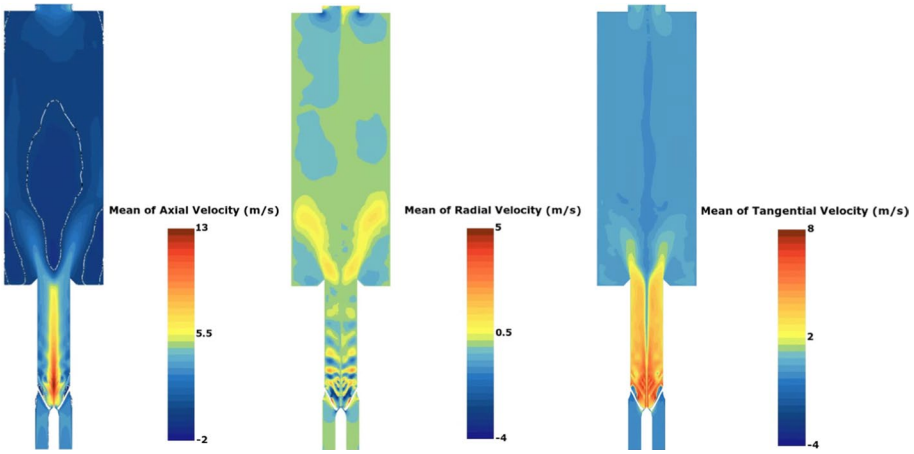

Fig. 10 Averaged velocity components for non-reacting flow with Re = 10 k. The components are from left to right: axial, radial and tangential. Isolines on the axial velocity contour demarcate the 0 m/s border

Fig. 10. The real recirculation zones (see Fig. 15) are slightly larger since the axial velocity will also attain positive values inside the recirculation zones. An example of the instantaneous axial velocity field at 3.5 s of physical time is shown next to the averaged axial velocity in Fig. 11.

To better understand the flow created after the swirler, an iso-surface based on the averaged axial velocity was created and shown in Fig. 12A. After the swirler, the flow has a clear helical structure similar to that discussed in ref. (Guo et al. 2002) for sudden expansion pipe flows. In Fig. 12B the instantaneous Q-criterion has been used to identify coherent structures of the flow. Immediately after the inlet to the combustion chamber, a large quantity of small size structures can be seen as in (Faler and Leibovich 1977; Subash et al. 2020), indicating vortex breakdown. A vortex rope along the axis of the mixing tube can also be identified in (B). Figure 12C shows a magnified view of (B) at the inlet to the combustion chamber. A precessing vortex core (PVC) (Syred 2006) can be seen in the early combustion chamber, indicated by the red circle. The PVC will affect the dynamics and stabilisation of the flame in the reactive cases.

4.2 Reactive Flow Results

The compositions used for the reactive cases can be seen in Table 1. The undiluted composition was representative of the syngas from black liquor gasification after gas cleaning to remove the acid gas species (H_2S, CO_2 and COS) from the syngas. For brevity the velocity comparison with experiments is only shown for SYN0 in Fig. 13 for Re 10 k but this result is representative of all three dilution cases. The predicted axial and horizontal velocity agree excellently with the experiments at low axial positions, but for higher axial positions the experimental and numerical results increasingly deviate from each other. The positions and magnitude of the peaks of the axial velocity are predicted well, except for 50 mm above the inlet where small discrepancies are visible. The horizontal velocity matches excellently with the experimental values with the exception of a small underprediction of peak velocity values.

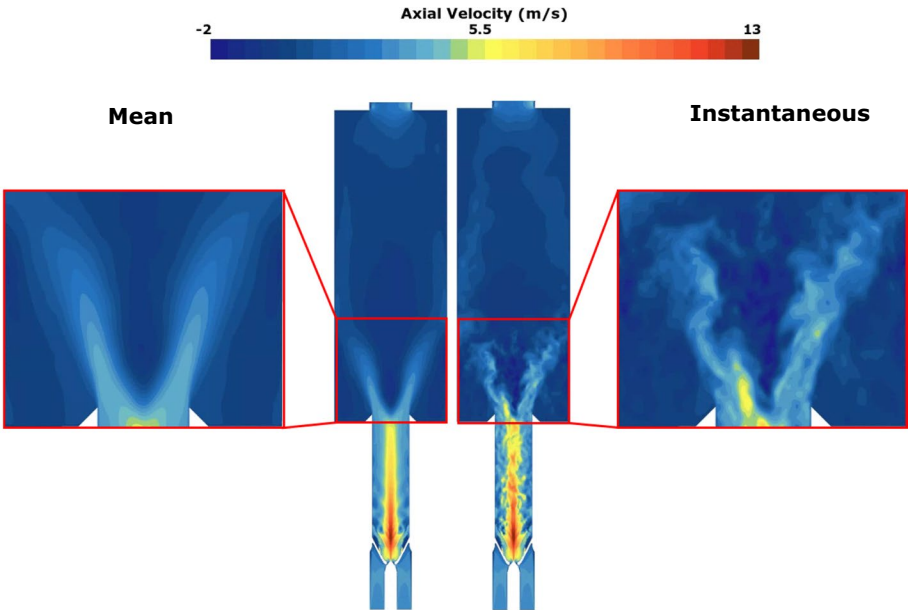

Fig. 11 Cold flow averaged axial velocity (left) and instantaneous axial velocity (right)

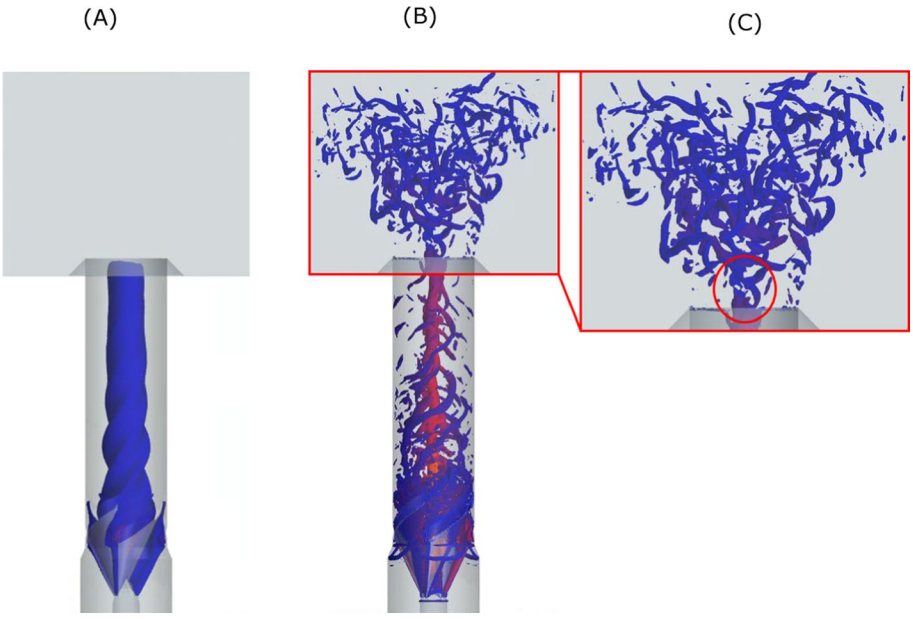

Fig. 12 Iso-surface of mean axial velocity showing the corkscrew structure of the flow (**A**), instantaneous Q-criterion to identify coherent structures of the flow as the vortex rope (**B**), magnified view of (**B**) illustrating coherent structures in the combustion chamber (**C**)

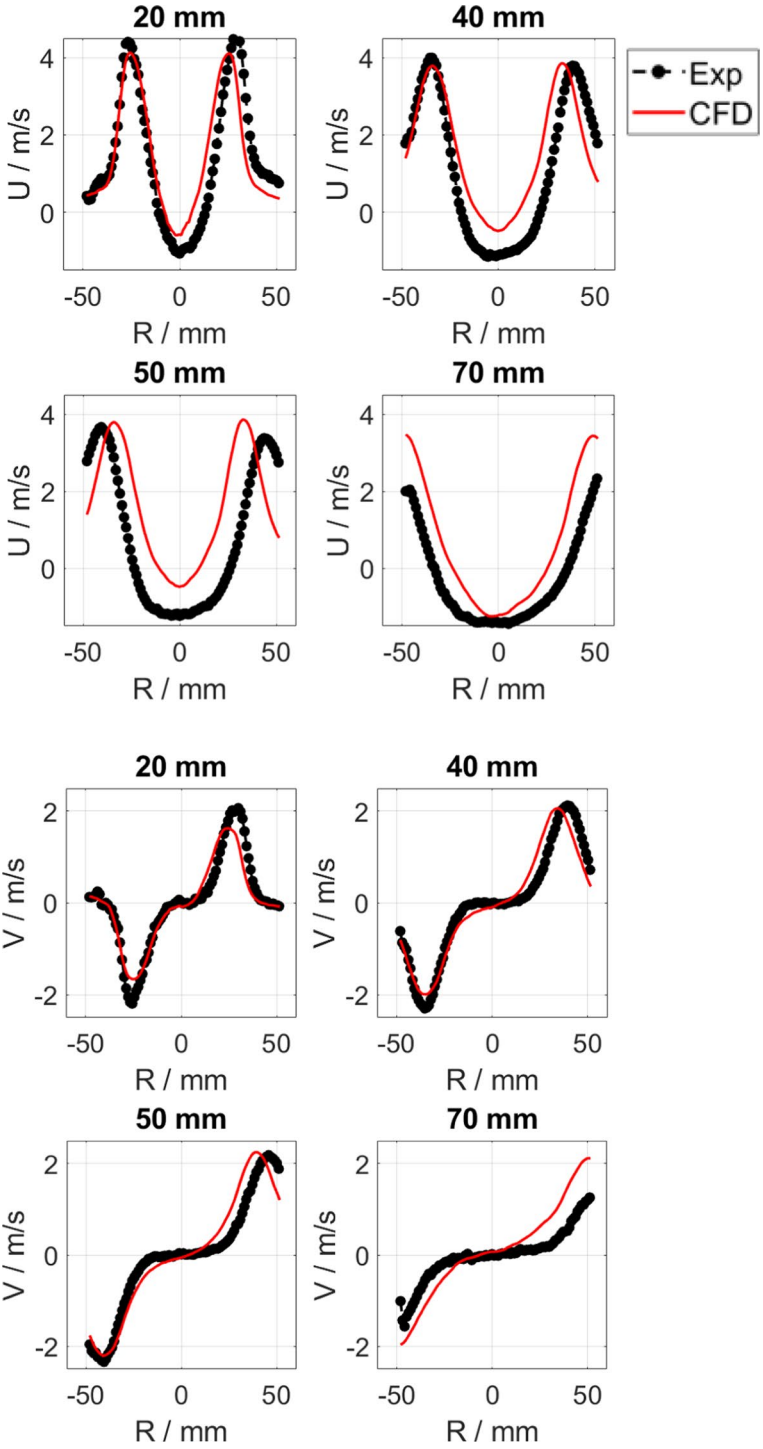

Fig. 13 Averaged axial and horizontal velocity comparison of LES and experiments at different axial positions

PIV data for Re 20 k only exists for SYN0. It is assumed based on the Re 10 k cases that the other dilutions will behave in a similar way and that the agreement between PIV and simulations for SYN0 is representative for those as well. Figure 14 shows the velocity comparison between simulations and experiments at Re 20 k. The positions and magnitude of the peak positive vertical velocity peaks are predicted well. However, for axial positions higher than 20 mm from the burner mouth the negative peak vertical velocities (found in the IRZ) are underpredicted by the model, similarly to the Re = 10 k cases. For the horizontal velocity comparison, it seems that the trends are captured well by the simulation. Also, the results follow a similar trend to the horizontal velocity comparison for the Re 10 k cases where peaks are underpredicted for all heights besides 70 mm above the burner mouth. Here the model has similar behaviour in its prediction of trends both for the 10 k and the 20 k Reynolds number cases.

Figure 15 shows the flow field comparison between all reactive cases. The flow field is represented by streamlines in a midplane of the domain, coloured by the normalised OH mole fraction. This was done to show the position of the flame front relative to the flow structures (more on flame front position in the following section). In this qualitative comparison, the model predicts a narrower IRZ and larger ORZ with increasing Reynolds number. However, even if the IRZ is narrower for the higher Reynolds number cases it experiences higher axial velocity values. In addition, the larger ORZ seem to affect the outer edges of the flame helping them to propagate further upstream, towards the fresh reactants, effectively thickening the flame at those areas with increasing Re. Moreover, the shape indicated by the zero-axial velocity isolines leads to an underprediction of the size of the recirculation zones. In addition, the pinched lower end of the IRZ of Fig. 10 does not appear in Fig. 15. Thus, care should be taken when analysing the flame position relative to the recirculation zone based solely on one velocity component. In addition, Fig. 16 shows PLIF and PIV data for all three dilutions at Re = 10 k (Pignatelli et al. 2023). The experimental interrogation window starts at approximately 2 mm above the burner mouth (Pignatelli et al. 2023); thus, the lower end of the flame is cut off. Experiments predict a V-shape flame as can be seen in Fig. 16, simulations on the other hand predict an unattached M-shape (Liu et al. 2021). The experimental results are limited to Re 10 k, it is probable that for higher Reynolds numbers a M-shape flame would be encountered experimentally as well. The shape difference with the simulations for Re = 10 k is minimal but can be clearly seen for higher Re. In the present paper, the flame front was identified based on the OH mole fraction, taking a range of 40–80% of its maximum value (Papafilippou et al. 2022). The opening angle of these flames has been computed based on OH both for experiments and simulations for Re 10 k. The simulations predict slightly narrower flames differing by a maximum of 13%.

Figure 17 shows the normalised OH mass fraction in grayscale for all the cases. Superimposed on that are isolines of the normalised heat release. It is clear that the heat release coincides perfectly with the position of the OH mass fraction. In this perfectly premixed case, the heat losses due to the thermal specification on the walls affect the heat release and hence the shape of the flame. With the use of adiabatic walls, the resulting flame would have an M-shape and both the OH mass fraction and heat release in Fig. 16 would reach the burner mouth.

Figure 18 shows a 2D projection of the 3D flame fronts based on the normalised OH mole fraction. The flame fronts for the lower Reynolds number cases are almost identical. The annulus of the flames (the outer legs on the 2D view in Fig. 14) dramatically thickens with increasing Reynolds number. SYN0 shows an almost 50% thicker outer flame in the Re 25 k case compared to the 10 k version. SYN34 has the smallest

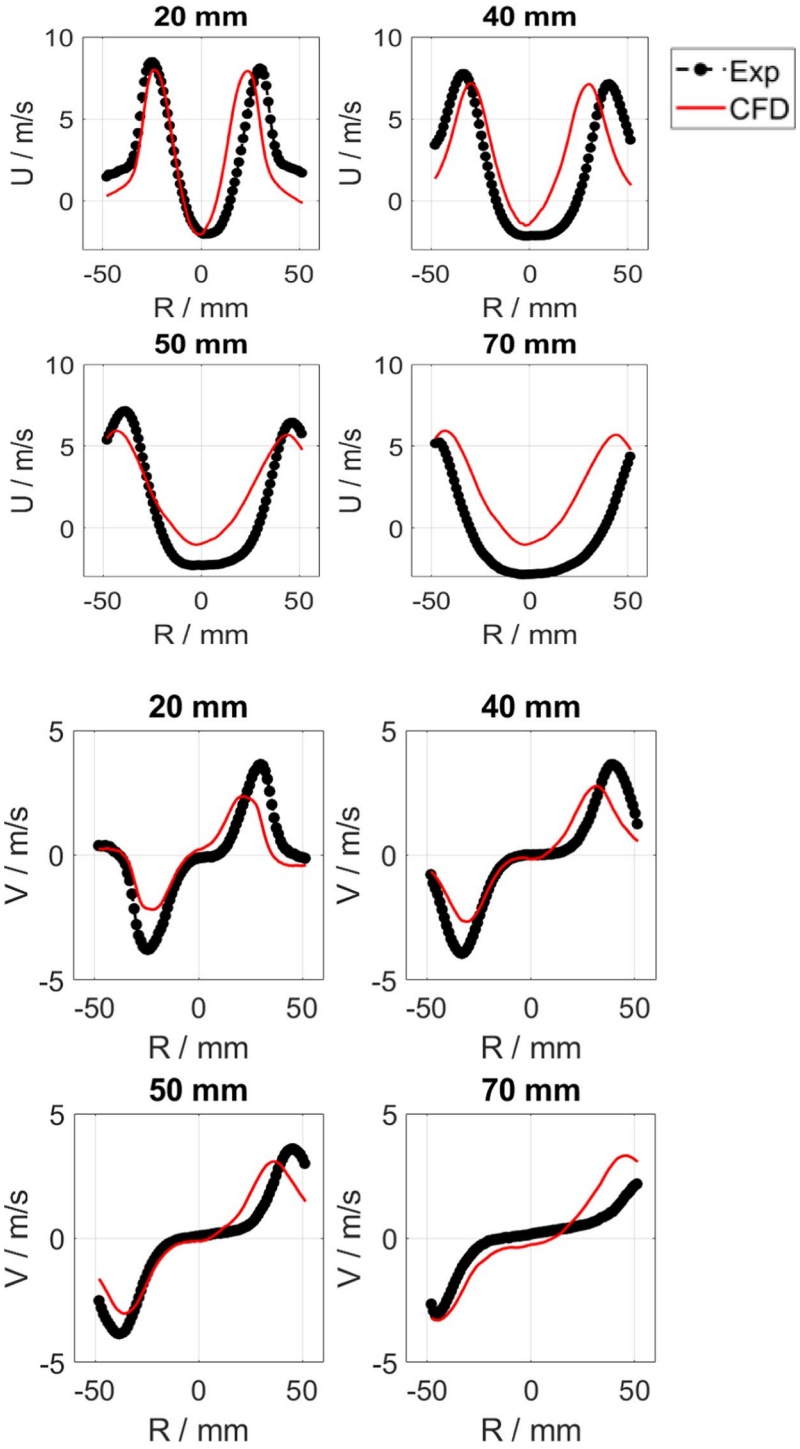

Fig. 14 Averaged axial and horizontal velocity comparison of LES and experiments at different axial positions for Re = 20 k

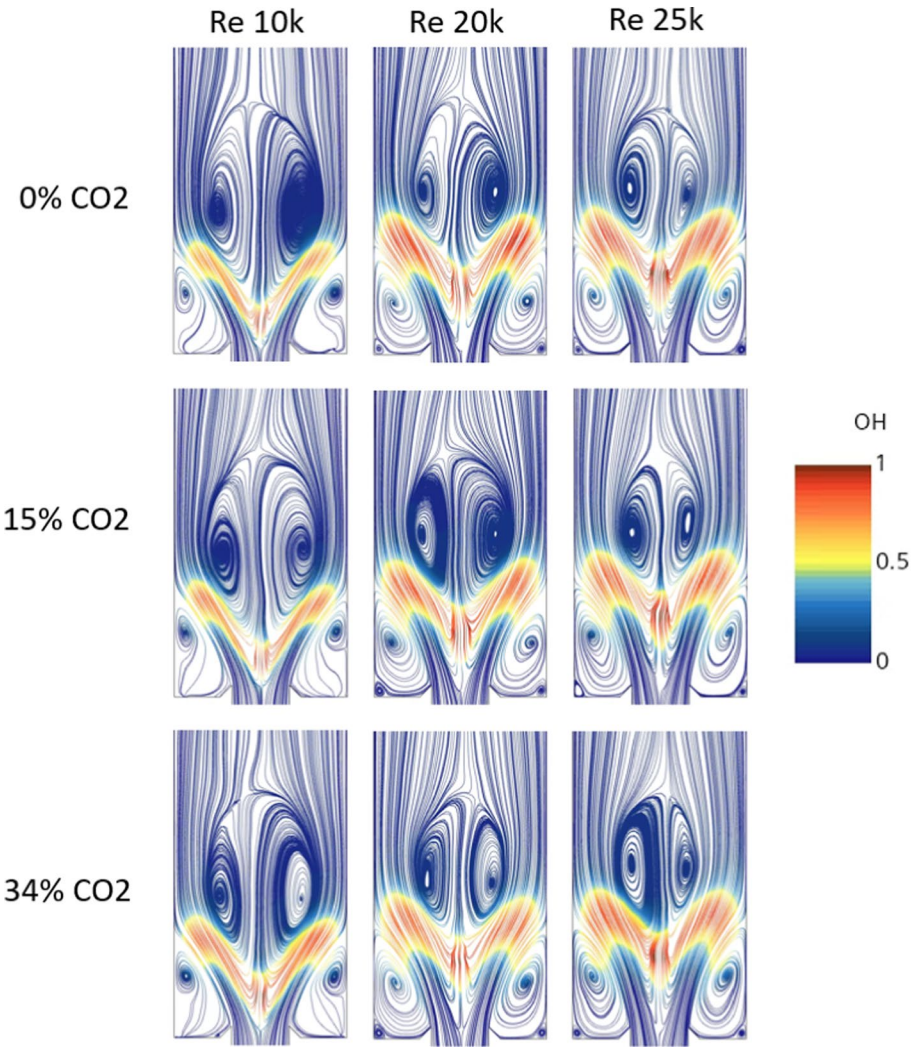

Fig. 15 Flow streamlines for three CO_2 dilutions (0%, 15% and 34% CO_2) and three Reynolds numbers (10 k, 20 k and 25 k)

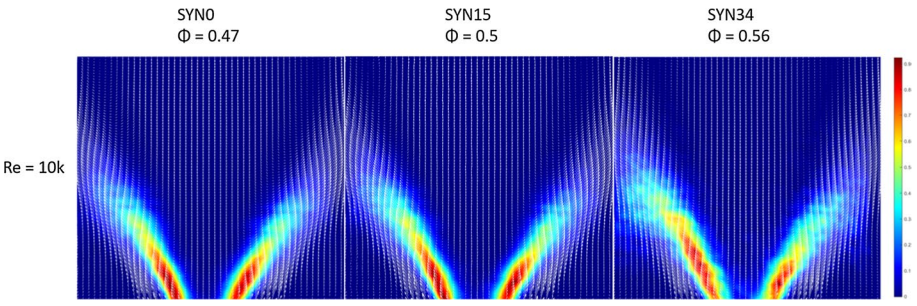

Fig. 16 PIV and OH-PLIF for all three CO_2 dilutions (0%, 15% and 34% CO_2) at Re = 10 k

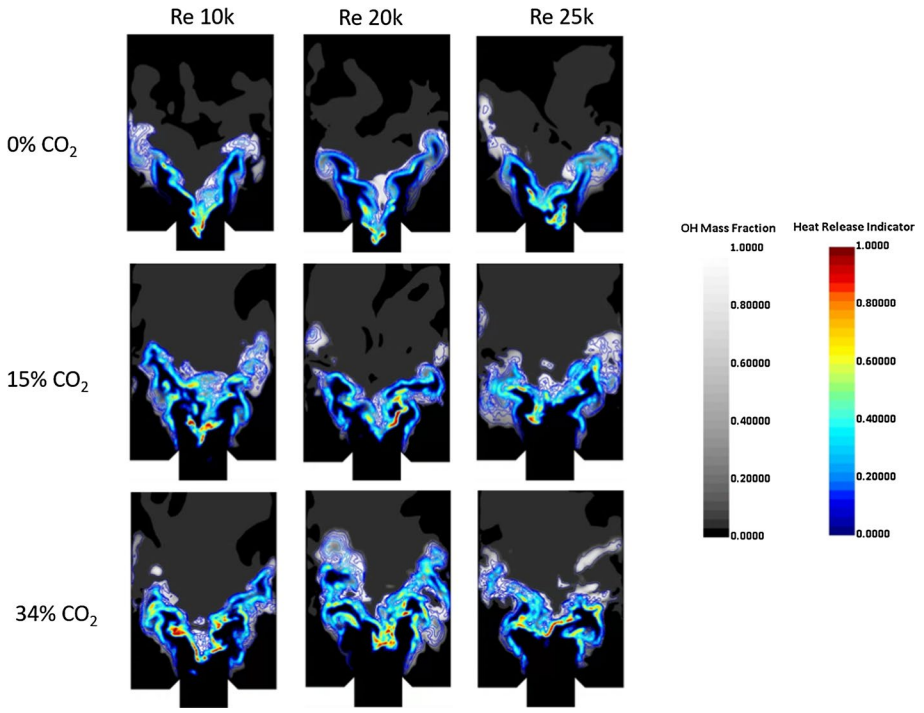

Fig. 17 Heat release iso-lines superimposed on the normalised OH mass fraction for all cases considered

percentage increase in annulus thickness at 32% compared with its Re 10 k version and SYN15 lies in between. Nonetheless, SYN34 at Re 25 k has the thickest annulus overall at 78.5 mm. This case also experiences the greatest lift-off length. For flame lift-off there are several definitions that have been proposed in the literature (Cabra et al. 2005; Cao et al. 2005; Gordon et al. 2007; Benim et al. 2019). Here, the definition by Cabra as defined in reference (Cao et al. 2005) is used. Where the liftoff distance is the height from the burner mouth up until the point that a mean OH mass fraction value of 0.0002 is encountered. SYN34 at Re 25 k experiences a liftoff height of 23.5 mm. Its Re 10 k counterpart stabilises exactly on the burner mouth. That was expected as SYN34 has the lowest laminar flame speed of all the cases considered here, hence, it is more difficult for this composition, at the studied equivalence ratio, to balance an increased momentum of incoming flow. This is a direct consequence of CO_2 dilution retarding the flame (Lieuwen et al. 2009). Consequently, the liftoff distance at Re 25 k for SYN0 was the lowest observed at 17 mm and for SYN15 at 18.75 mm. Since liftoff is encountered close to the lean blowout limit (Liu et al. 2021), it was suspected that the Re 25 k cases should be close to the critical limit, especially for SYN34. An ad-hoc simulation without verification of Re 35 k for SYN34 was run to assess this assumption but blowout was not encountered.

An interesting observation in the experiments is that the flame has a pocket structure, showing a discontinuous flame with isolated pockets that increase in number with increasing percentage of CO_2 (Pignatelli et al. 2023).Unfortunately, this is not captured by the current model. A possible explanation for the pocket structure could

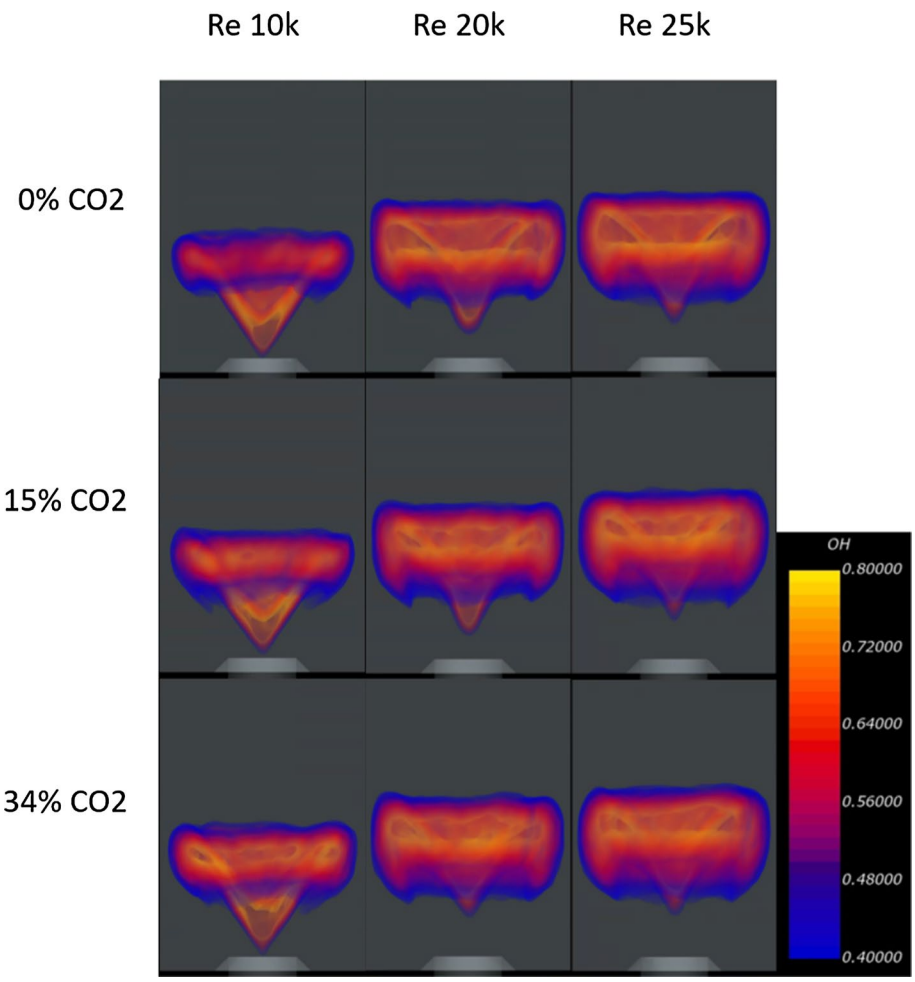

Fig. 18 Flame fronts based on the OH mole fraction for three CO_2 dilutions (0%, 15% and 34% CO_2) and three Reynolds numbers (10 k, 20 k and 25 k)

be preferential diffusion, which is possible to account for within the FGM model (Mukundakumar et al. 2021). This gives a more accurate depiction of non-unity Lewis number fuels (as is the case for hydrogen blends) and a more realistic depiction of lean hydrogen blend combustion behaviour. The corresponding effective Lewis number of the investigated fuels are 0.98, 1.46 and 1.9 for SYN0, SYN15 and SYN34 respectively (at the equivalence ratio shown in Table 1). Hence, it would be of interest to investigate this further in future work. Nonetheless, apart from the pocket structure the simulations compared well to the experiments, leading to a successful validation of the model. Furthermore, the predictions for SYN15 and SYN34 at Re 20 k where no experimental data was available seem reasonable (following the trends of SYN0 with supplied experimental data). From the verification, the validation and the reasonable trends at Re 20 k where no experimental data were available, it is likely that the cases at Re 25 k are reasonably predicted as well. Future work will focus on the flammability

limits (flashback and blowout) and the effect of preferential diffusion to further assess the applicability of the model and its performance against experimental data.

5 Conclusions

The CeCOST swirl burner was investigated using LES simulations, for different levels of CO_2 in the syngas mixture and three Reynolds numbers, with a FGM sub-model for combustion modelling. The fluid dynamics model was assessed in a separate step against cold flow experiments. In this comparison the overall agreement with measurements were very good with the shape of the velocity profiles at different heights predicted excellently but with the peak values slightly overpredicted by the LES model. In addition, clear signs of a vortex rope and a precessing vortex core near the flame zone were found.

To assess the quality of the numerical scheme and the sub-grid scale turbulence model two different quality measures, the LES_IQ and a single grid estimator, were used. In this evaluation it was found that the grid with 6 million cells resulted in a proper LES where more than 70% of the turbulent energy was resolved, with the exception of small areas near the tip of the swirler, near the walls and close to the outlet. For the reactive flow an assessment was done by comparison to experiments with three syngas compositions that were obtained by diluting a base case mixture of H_2 and CO with different amounts of CO_2. The equivalence ratios were selected to give the same adiabatic flame temperature of approximately 1600 K in all three cases. The corresponding laminar flame speeds were almost identical for all three gas mixtures, but with a slightly lower flame speed for SYN34. Experimental data were available for all three dilutions at Re 10 k and for one case (SYN0) at Re 20 k. Judging from the similarity of the cases at Re 10 k, the predictions at Re 20 k seem reasonable and in line with SYN0. Consequently, confidence was built for the predictions at Re 25 k.

The flow patterns of the reactive simulations were found to be sensitive to the Reynolds number, with the higher Re simulations predicting a narrower inner recirculation zone with higher velocity magnitude and a larger outer recirculation zone. In addition, the outer recirculation zones enlarge with increasing Re, aiding the edges of the flame to propagate upstream.

Flame opening angle comparisons with experiments show a difference of 13%. The flame lift-off in this work was judged based on the flame front distance from the burner mouth. The flame with the highest lift-off was also the one with the lowest laminar flame speed (SYN34, 18 cm/s). This is an expected outcome since a flame with lower laminar flame speed will be less capable than flames with higher laminar flame speeds to balance the incoming flow. Furthermore, with increasing Re the outer annulus of the flames gets thicker. This can be explained by the increased outer recirculation aiding the flame in propagating upstream. The case with the highest increase in annulus thickness was SYN0, experiencing a 50% increase in thickness when compared to the Re 10 k and Re 25 k counterparts. At Re 25 k the liftoff distance was the highest for SYN34 followed by SYN15 and SYN0. An exploratory ad-hoc simulation showed that even though a significant liftoff is encountered the cases were not close to the critical blowout limit.

The major discrepancy compared to experiments is that the flame pocket structure that was seen in experiments was not captured by the simulations. It is assumed that the reason is the lack of preferential diffusion in the model. Despite that, the experiments were

reasonably predicted by the simulations. To further assess the performance of the current model, a flammability limit study will be conducted in the near future.

Acknowledgements The financial support from the Swedish Biomass Gasification Centre SFC, which is funded by the Swedish Energy Agency and a consortium of companies, is acknowledged. The simulations were performed on resources (Dardel) provided by the National Academic Infrastructure for Supercomputing in Sweden (NAISS) at PDC partially funded by the Swedish Research Council through Grant agreement *No. 2016-07213*. The authors thank all the staff of PDC for their technical assistance.

Author contributions N.P. had a main role in conceptualisation, performed the simulations, analysed the results, created the Figures and wrote the manuscript with the aid of the co-authors.F.P. helped in conceptualisation, aided in the analysis of the results, provided PIV data for Figures 7,8, 12 and 13, created Figure 15 and provided experimental insight.A.A.S. helped in conceptualisation, aided in the analysis of the results and provided experimental insight.M.A.C. helped in conceptualisation.R.G. had a main role in conceptualisation, aided in the analysis of the results and writing of the manuscript, provided numerical insight. All authors have critically reviewed the manuscript prior to its submission

Funding Open access funding provided by Lulea University of Technology.

Declarations

Conflict of interest The authors have no conflict of interests to declare.

Open Access This article is licensed under a Creative Commons Attribution 4.0 International License, which permits use, sharing, adaptation, distribution and reproduction in any medium or format, as long as you give appropriate credit to the original author(s) and the source, provide a link to the Creative Commons licence, and indicate if changes were made. The images or other third party material in this article are included in the article's Creative Commons licence, unless indicated otherwise in a credit line to the material. If material is not included in the article's Creative Commons licence and your intended use is not permitted by statutory regulation or exceeds the permitted use, you will need to obtain permission directly from the copyright holder. To view a copy of this licence, visit http://creativecommons.org/licenses/by/4.0/.

References

Benim, A.C., et al.: Computational investigation of a lifted hydrogen flame with LES and FGM. Energy **173**, 1172–1181 (2019). https://doi.org/10.1016/j.energy.2019.02.133

Cabra, R., et al.: Lifted methane-air jet flames in a vitiated coflow. Combust. Flame **143**(4), 491–506 (2005). https://doi.org/10.1016/j.combustflame.2005.08.019

Cao, R.R., Pope, S.B., Masri, A.R.: Turbulent lifted flames in a vitiated coflow investigated using joint PDF calculations. Combust. Flame **142**(4), 438–453 (2005). https://doi.org/10.1016/j.combustflame.2005.04.005

Carlsson, P., et al.: Experimental investigation of an industrial scale black liquor gasifier. 1. The effect of reactor operation parameters on product gas composition. Fuel **89**(12), 4025–4034 (2010). https://doi.org/10.1016/j.fuel.2010.05.003

Celik, I.B., Cehreli, Z.N., Yavuz, I.: Index of resolution quality for large eddy simulations. J. Fluids Eng. Trans. ASME **127**(5), 949–958 (2005). https://doi.org/10.1115/1.1990201

Celik, I., Klein, M., Janicka, J.: Assessment measures for engineering LES applications. J. Fluids Eng. Trans. ASME **131**(3), 0311021–03110210 (2009). https://doi.org/10.1115/1.3059703

Charlette, F., Meneveau, C., Veynante, D.: A power-law flame wrinkling model for LES of premixed turbulent combustion part I: non-dynamic formulation and initial tests. Combust. Flame **131**(1–2), 159–180 (2002). https://doi.org/10.1016/S0010-2180(02)00400-5

Dutta, R., Xing, T.: Five-equation and robust three-equation methods for solution verification of large eddy simulation. J. Hydrodyn. **30**(1), 23–33 (2018). https://doi.org/10.1007/s42241-018-0002-0

Endres, A., Sattelmayer, T.: Large eddy simulation of confined turbulent boundary layer flashback of premixed hydrogen-air flames. Int. J. Heat Fluid Flow **72**(6), 151–160 (2018). https://doi.org/10.1016/j.ijheatfluidflow.2018.06.002

Faler, J.H., Leibovich, S.: Disrupted states of vortex flow and vortex breakdown. Phys. Fluids **20**(9), 1385–1400 (1977). https://doi.org/10.1063/1.862033

Ferziger, J.H., Perić, M., Street, R.L.: Computational Methods for Fluid Dynamics, 4th edn. Springer Nature Switzerland, Cham (2019). https://doi.org/10.1007/978-3-319-99693-6

Freitag, M., Klein, M.: An improved method to assess the quality of large eddy simulations in the context of implicit filtering. J. Turbul. **7**, 1–11 (2006). https://doi.org/10.1080/14685240600726710

Geurts, B.J., Fröhlich, J.: A framework for predicting accuracy limitations in large-eddy simulation. Phys. Fluids (2002). https://doi.org/10.1063/1.1480830

Gicquel, L.Y.M., Staffelbach, G., Poinsot, T.: Large eddy simulations of gaseous flames in gas turbine combustion chambers. Prog. Energy Combust. Sci. **38**(6), 782–817 (2012). https://doi.org/10.1016/j.pecs.2012.04.004

Goodwin, D.G., Moffat, H.K., Speth, R.L.: Cantera: An Object-Oriented Software Toolkit for Chemical Kinetics, Thermodynamics, and Transport Processes (2016). Available at http://www.cantera.org

Gordon, R.L., et al.: Transport budgets in turbulent lifted flames of methane autoigniting in a vitiated co-flow. Combust. Flame **151**(3), 495–511 (2007). https://doi.org/10.1016/j.combustflame.2007.07.001

GRI-Mech 3.0 (no date). Available at http://combustion.berkeley.edu/gri-mech/version30/text30.html. Accessed 2 Oct 2018

Guo, B., Langrish, T.A.G., Fletcher, D.F.: CFD simulation of precession in sudden pipe expansion flows with low inlet swirl. Appl. Math. Model. **26**(1), 1–15 (2002). https://doi.org/10.1016/S0307-904X(01)00041-5

Higman, C., van der Burgt, M. Gasification. Edited by 2. Elsevier (2008). Available at https://shop.elsevier.com/books/gasification/higman/978-0-7506-8528-3

Jafri, Y., et al.: Multi-aspect evaluation of integrated forest-based biofuel production pathways: Part 2. Economics, GHG emissions, technology maturity and production potentials. Energy **172**, 1312–1328 (2019). https://doi.org/10.1016/j.energy.2019.02.036

Klein, M.: An attempt to assess the quality of large eddy simulations in the context of implicit filtering. Flow Turbul. Combust. **75**(1–4), 131–147 (2005). https://doi.org/10.1007/s10494-005-8581-6

Landälv, I., et al.: Two years experience of the BioDME project—a complete wood to wheel concept. Envron. Prog. Sustain. Energy (2014). https://doi.org/10.1002/ep.11993

Legier, J.P., Poinsot, T., Veynante, D: Dynamically thickened flame LES model for premixed and non-premixed turbulent combustion. In: Proceedings of the Summer Program, Centre for Turbulence Research, pp. 157–168 (2000)

Lehtiniemi, H., et al.: Modeling diesel spray ignition using detailed chemistry with a progress variable approach. Combust. Sci. Technol. **178**(10–11), 1977–1997 (2006). https://doi.org/10.1080/00102200600793148

Li, S., et al.: Effects of inert dilution on the lean blowout characteristics of syngas flames. Int. J. Hydrog. Energy **41**(21), 9075–9086 (2016). https://doi.org/10.1016/j.ijhydene.2016.02.099

Lieuwen, T., Yang, V., Yetter, R. (eds.): Synthesis Gas Combustion, Synthesis Gas Combustion. Taylor and Francis, Milton Park (2009)

Liu, X., et al.: Investigation of turbulent premixed methane/air and hydrogen-enriched methane/air flames in a laboratory-scale gas turbine model combustor. Int. J. Hydrog. Energy **46**(24), 13377–13388 (2021). https://doi.org/10.1016/j.ijhydene.2021.01.087

Meyers, J., Geurts, B.J., Baelmans, M.: Database analysis of errors in large-eddy simulation. Phys. Fluids **15**(9), 2740–2755 (2003). https://doi.org/10.1063/1.1597683

Mira, D., et al.: Numerical investigation of a lean premixed swirl-stabilized hydrogen combustor and operational conditions close to flashback. In: Proceedings of the ASME Turbo Expo, p. 13 (2018). https://doi.org/10.1115/GT2018-76229.

Mukundakumar, N., et al.: A new preferential diffusion model applied to FGM simulations of hydrogen flames. Combust. Theory Model **25**(7), 1245–1267 (2021). https://doi.org/10.1080/13647830.2021.1970232

Nicolai, H., et al.: Flamelet LES of swirl-stabilized oxy-fuel flames using directly coupled multi-step solid fuel kinetics. Combust. Flame **241**, 112062 (2022). https://doi.org/10.1016/j.combustflame.2022.112062

Papafilippou, N., Chishty, M.A., Gebart, R.: On the flame shape in a premixed swirl stabilised burner and its dependence on the laminar flame speed. Flow Turbul. Combust. **108**(2), 461–487 (2022). https://doi.org/10.1007/s10494-021-00279-6

Papafilippou, N., Chishty, M.A., Gebart, R.: Systematic assessment of the two-step, one-way coupled method for computational fluid dynamics. ASME Open J. Eng. **2**, 1–11 (2023). https://doi.org/10.1115/1.4062111

Pignatelli, F., et al.: Effect of CO_2 dilution on structures of premixed syngas/air flames in a gas turbine model combustor. Combust. Flame **255**, 112912 (2023). https://doi.org/10.1016/j.combustflame.2023.112912

Pillai, A.L., et al.: Investigation of combustion noise generated by an open lean-premixed H_2/air low-swirl flame using the hybrid LES/APE-RF framework. Combust. Flame **245**, 112360 (2022). https://doi.org/10.1016/j.combustflame.2022.112360

Pitsch, H.: Large-eddy simulation of turbulent combustion. Annu. Rev. Fluid Mech. **38**, 453–482 (2006). https://doi.org/10.1146/annurev.fluid.38.050304.092133

Poinsot, T., Veynante, D.: Theoretical and Numerical Combustion, 2nd edn. RT Edwards, Inc, Morningside (2005)

Pope, S.B.: Turbulent Flows. Cambridge Universtiy Press, Cambridge (2000). https://doi.org/10.1017/CBO9780511840531

Samiran, N.A., et al.: 'Swirl stability and emission characteristics of CO-enriched syngas/air flame in a premixed swirl burner. Process Saf. Environ. Protect. **112**, 315–326 (2017). https://doi.org/10.1016/j.psep.2017.07.011

Samiran, N.A., et al.: Experimental and numerical studies on the premixed syngas swirl flames in a model combustor. Int. J. Hydrog. Energy **44**(44), 24126–24139 (2019). https://doi.org/10.1016/j.ijhydene.2019.07.158

Simcenter STAR-CCM+ User Guide (2020). Available at: https://docs.sw.siemens.com/en-US/product/226870983/doc/PL20201113103827399.starccmp_userguide_html/custom/ (Accessed: 10 October 2019).

Subash, A.A., et al.: Flame investigations of a laboratory-scale CECOST swirl burner at atmospheric pressure conditions. Fuel **279**(2), 118421 (2020). https://doi.org/10.1016/j.fuel.2020.118421

Syred, N.: A review of oscillation mechanisms and the role of the precessing vortex core (PVC) in swirl combustion systems. Prog. Energy Combust. Sci. **32**(2), 93–161 (2006). https://doi.org/10.1016/j.pecs.2005.10.002

Taamallah, S., et al.: 'Fuel flexibility, stability and emissions in premixed hydrogen-rich gas turbine combustion: technology, fundamentals, and numerical simulations. Appl. Energy **154**, 1020–1047 (2015). https://doi.org/10.1016/j.apenergy.2015.04.044

van Oijen, J.A., et al.: 'State-of-the-art in premixed combustion modeling using flamelet generated manifolds. Prog. Energy Combust. Sci. **57**, 30–74 (2016). https://doi.org/10.1016/j.pecs.2016.07.001

Vervisch, L., et al.: Scalar energy fluctuations in large-eddy simulation of turbulent flames: statistical budgets and mesh quality criterion. Combust. Flame **157**(4), 778–789 (2010). https://doi.org/10.1016/j.combustflame.2009.12.017

Williams, F.A.: Combustion Theory. CRC Press, Boca Raton (1994)

Publisher's Note Springer Nature remains neutral with regard to jurisdictional claims in published maps and institutional affiliations.